

The Intrinsic Stochasticity of the ⁵⁶Ni Distribution of Single-Degenerate Type Ia Supernovae

CHRIS BYROHL,¹ ROBERT FISHER,² AND DEAN TOWNSLEY³

¹*Max-Planck-Institut für Astrophysik, Karl-Schwarzschild-Straße 1, 85748 Garching, Germany*

²*Department of Physics, University of Massachusetts Dartmouth, 285 Old Westport Road, North Dartmouth, Ma. 02740, USA*

³*Department of Physics & Astronomy, Box 870324, University of Alabama, Tuscaloosa, AL. 35487-0324, USA*

ABSTRACT

Binary Chandrasekhar-mass white dwarfs accreting mass from non-degenerate stellar companions through the single-degenerate channel have reigned for decades as the leading explanation of Type Ia supernovae. Yet, a comprehensive theoretical explanation has not yet emerged to explain the expected properties of the canonical near-Chandrasekhar-mass white dwarf model. A simmering phase within the convective core of the white dwarf leads to the ignition of one or more flame bubbles scattered across the core. Consequently, near-Chandrasekhar-mass single-degenerate SNe Ia are inherently stochastic, and are expected to lead to a range of outcomes, from subluminous SN 2002cx-like events, to overluminous SN 1991T-like events. However, all prior simulations of the single-degenerate channel carried through the detonation phase have set the ignition points as free parameters. In this work, for the first time, we place ignition points as predicted by *ab initio* models of the convective phase leading up to ignition, and follow through the detonation phase in fully three-dimensional simulations. Single-degenerates in this framework are characteristically overluminous. Using a statistical approach, we determine the ⁵⁶Ni mass distribution arising from stochastic ignition. While there is a total spread of $\gtrsim 0.2M_{\odot}$ for detonating models, the distribution is strongly left-skewed, and with a narrow standard deviation of $\simeq 0.03M_{\odot}$. Conversely, if single-degenerates are not overluminous but primarily yield normal or failed events, then the models require fine-tuning of the ignition parameters, or otherwise require revised physics or progenitor models. We discuss implications of our findings for the modeling of single-degenerate SNe Ia.

Keywords: supernovae: general — supernovae: individual (1991T, 2002cx) — hydrodynamics — white dwarfs

1. INTRODUCTION

Numerous classic works identified white dwarfs accreting to near the Chandrasekhar mass M_{ch} in binary systems as candidate progenitors of Type Ia supernovae (SNe Ia) – e.g. Arnett (1969), Whelan & Iben (1973), and Nomoto et al. (1984). This classic picture was long thought to provide an explanation for the uniformity of brightnesses observed in SNe Ia (Phillips 1993).

The nature of the dominant production channel for SNe Ia has long been unclear (Branch et al. 1995) and more recently, the classic picture of near M_{ch} progenitors has been substantially revised, with single-degenerates now widely believed to be rare in nature. The single-degenerate channel has been shown to be inconsistent with a range of constraints, including the delay-time distribution, the absence of hydrogen, and the absence of companions (Maoz et al. 2014). Single-degenerates are also inconsistent with observational and theoretical

rate predictions (Maoz & Mannucci 2012). However, recent observations have provided strong evidence that Chandrasekhar-mass white dwarf SNe Ia do occur in at least some systems in nature. Hard X-ray spectra of the 3C 397 supernova remnant (SNR) are consistent with electron captures which arise during nuclear burning at high densities typical of Chandrasekhar-mass white dwarfs (Yamaguchi et al. 2014, 2015). Additional X-ray and infrared observations of the Kepler SNR suggest that it was an overluminous single-degenerate supernova (Katsuda et al. 2015). Furthermore, the pre-maximum light shock signature detected in both a subluminous SN Ia 2012cg (Marion et al. 2016) and a normal SN Ia iPTF14atg (Cao et al. 2015) similar to theoretical predictions of the shock interaction with the companion star (Kasen 2010), although these observations have also been contested (Kromer et al. 2016; Shappee et al. 2018).

A large body of theoretical and computational work has explored possible mechanisms for single-degenerate SNe Ia (Maoz & Mannucci 2012). Many single-degenerate explosion mechanisms begin with a deflagration in the convective core of a near- M_{Ch} WD (Nomoto et al. 1984). From this common starting point, authors have explored the possibility of pure deflagrations (Röpke et al. 2007a; Jordan et al. 2012; Kromer et al. 2013), deflagration-to-detonation transitions (DDTs) (Khokhlov (1991); Röpke et al. (2007b); Seitenzahl et al. (2013); Malone et al. (2014); Martínez-Rodríguez et al. (2017); Dave et al. (2017) and many more, and gravitationally-confined detonations (GCDs) (Plewa et al. 2004; Röpke et al. 2007b; Townsley et al. 2007; Jordan et al. 2008; Meakin et al. 2009; Seitenzahl et al. 2016). The viability of the proposed explosion mechanisms hinges crucially on the nature of the flame ignition during the convective phase. In particular, the GCD mechanism relies upon an offset ignition to buoyantly drive the flame bubble through breakout. Because the vigor of the GCD mechanism relies upon maintaining the WD intact until the ash collides at a point opposite of breakout, its viability is diminished as the ignitions become more centrally concentrated and multi-point. In contrast, a pure deflagration model produces good agreement with observations of the subclass of SNe Iax (Kromer et al. 2013), but requires a vigorous deflagration phase with several simultaneous near-central ignitions. Both the pure deflagration and the GCD mechanism require that the flame surface does not undergo a transition to a detonation prior to breakout, as the DDT model does. Furthermore, there exists the possibility that a detonation does not arise during the initial ash collision subsequent to breakout, and that the WD remains gravitationally bound, leading to a subsequent contraction and a detonation through the pulsationally-assisted GCD (PGCD) mechanism (García-Senz & Bravo 2005; Jordan et al. 2012).

Because the ignition of a flame bubble in the convective core of the white dwarf is inherently stochastic, outcomes ranging from subluminous through overluminous SNe Ia are expected to arise in Chandrasekhar-mass SNe Ia. The ignition arises within a highly-turbulent (Reynolds number $\text{Re} \sim 10^{15}$) convective flow (Isern et al. 2017), with the detailed outcome critically dependent upon the high-end tail of the temperature distribution. For many years, the distribution of ignition points was poorly constrained by theory and simulation (García-Senz & Woosley 1995; Woosley et al. 2004). Early studies suggested multi-point ignitions as a viable scenario, which has only been revised recently as it became possible to begin to simulate these crucial last

minutes of the simmering phase in full 3D simulations. For example, Zingale et al. (2011) and Nonaka et al. (2012) performed a numerical study for a WD with a central density $2.2 \times 10^9 \text{ g cm}^{-3}$ and central temperature $6.25 \times 10^8 \text{ K}$ to determine the probability distribution of hot spots triggering the deflagration phase. Zingale et al. (2011) demonstrated that most ignitions for the progenitor considered occur at a single point at radial offsets below 100 km from the center, and most likely at about 50 km. Consequently, these *ab initio* simulations point towards a low amount of deflagration energy resulting from a small single bubble, buoyancy-driven ignition, in contrast to prior simulations which often invoked multiple-bubble ignitions. It has been known for some time that such low-deflagration energies generally lead to large amounts of Röpke et al. (2007b) run a series of simulations with off-centered ignitions demonstrating an anti-correlation of deflagration yield and ignition offset. However, initial offsets do not include ignitions below 50 km, thus neglecting roughly half of the ignitions expected from results in Nonaka et al. (2012). Hillebrandt et al. (2007) propose that off-centered, lob-sided explosions, such as those following the deflagration phase simulated in Röpke et al. (2007b), might explain overluminous SN Ia events.

Recent theoretical work explored the physics of stochastic ignition close to the WD’s center using semi-analytic methods in-depth, and demonstrated that single-bubble ignitions are generally buoyancy-dominated, leading to a weak deflagration phase (Fisher & Jumper 2015). Consequently, as Fisher & Jumper (2015) argued, single-bubble ignitions tend to lead to the production of a relatively large amount of ^{56}Ni and hence an overluminous SN Ia. This theoretical work was soon given observational support when spectral modeling of the nebular phase of SNe Ia revealed the canonical bright event SN 1991T had an inferred ejecta mass of $1.4 M_{\odot}$ (Childress et al. 2015). Most recently, Jiang et al. (2018) have examined the early-phase light curves of 40 SNe Ia in the optical, UV, and NUV, and demonstrated that all six luminous 91T- and 99aa-like events in their sample are associated with an early-excess consistent with a ^{56}Ni -abundant outer layer, as expected in the GCD scenario. Subsequent three-dimensional simulations of a buoyantly-driven single bubble ignition confirmed a large amount of ^{56}Ni consistent with SN 1991T (Seitenzahl et al. 2016). However, because the stable IGEs tend to be buoyantly-driven in the GCD model, Seitenzahl et al. (2016) found that the observed stable IGEs at low velocities in their model could only be reproduced along a line of sight centered around the detonation region. While there are systemic differences

in how the LEAFS code used by Seitenzahl et al. (2016) treats subgrid scale turbulent nuclear burning in comparison to FLASH – see e.g. Jordan et al. (2008), it is possible that the bulk of this inconsistency could be rectified by a DDT as opposed to a GCD model. In particular, Fisher & Jumper (2015) noted that buoyantly-driven ignitions will lead to a large amount of ^{56}Ni and an overluminous SNe Ia in both the DDT and GCD models.

This recent observational and theoretical progress motivates the current study, in which we explore the inherent stochasticity of near-Chandrasekhar mass white dwarfs in the single-degenerate channel, from ignition through detonation. In Section 2, we shortly summarize the simulation setup and the assumed initial hot spot distribution. In Section 3, we describe the WD’s evolution from ignition to its possible detonation depending on the ignition’s offset to the center of mass and link our findings to the initial hot spot distribution. In Section 4, we discuss possible uncertainties in our modeling before summarizing our findings in Section 5.

2. METHODOLOGY

Our simulations were performed with the 3D Eulerian adaptive mesh refinement (AMR) code FLASH 4.3 (Fryxell et al. 2000) solving the hydrodynamic equation with the directionally split piecewise-parabolic method (PPM). We use a tabular Helmholtz equation of state taking into account radiation, nuclei, electrons, positrons and corrections for Coulomb effects, which remains valid in the electron degenerate relativistic regime (Timmes & Swesty 2000). Flame physics is modeled by an advection-diffusion-reaction equation. Nuclear energy generation is incorporated using a simplified treatment of the flame energetics (Townsend et al. 2007, 2009, 2016). Self-gravity is accounted for by a multipole solver (Couch et al. 2013) up to order $l = 6$ with isolated boundary conditions.

The progenitor model of the white dwarf used assumes a mass of $1.38 M_{\odot}$ and a uniform 50/50 carbon/oxygen (C/O) composition. See Section 4 for a discussion of the impact of non-zero stellar progenitor metallicity. The white dwarf has a central temperature stratification, including an adiabatic core with central density $2.2 \times 10^9 \text{ g cm}^{-3}$ and temperature $7 \times 10^8 \text{ K}$, pressure-matched onto an isothermal envelope with temperature 10^7 K (Jackson et al. 2010; Krueger et al. 2012). Furthermore, the central density of our WD progenitor is a standard value commonly considered in the literature, because higher-central density WD progenitors produce anomalously high abundances of Fe-peak elements, including ^{48}Ca , ^{54}Cr , and ^{66}Zn (Meyer et al. 1996; Woosley 1997;

Nomoto et al. 1997; Brachwitz et al. 2000; Dave et al. 2017; Mori et al. 2018).

A very low density region surrounding the white dwarf, sometimes referred to in the literature as “fluff,” is required by Eulerian grid-based simulations, which cannot treat empty space without some matter density. The fluff is chosen to have an initial density of $10^{-3} \text{ g cm}^{-3}$ and temperature of $3 \times 10^7 \text{ K}$, and is dynamically unimportant for the duration of the models presented here.

Since the deflagration energy release and the nucleosynthetic yield of ^{56}Ni hinges critically on the bubble initial conditions, we investigate the earliest phases of the bubble evolution in Section 3.1. The turbulent cascade behaves fundamentally differently in 2D and 3D, and influences our choices in determining the spatial dimensionality of the simulations presented here. In particular, in 2D, the turbulent cascade is inverse, proceeding from smaller to larger scales (Kraichnan 1967). In contrast, in 3D, the turbulent cascade proceeds directly, from larger to smaller scales, where the energy is dissipated at the smallest scales due to viscosity. In the early-time simulations, the bubble remains laminar, and can be simulated in 2D. The fundamental distinctions between turbulence in 2D and 3D have major ramifications for studying longer timescales, on which the flame becomes fully turbulent, since physically-motivated flame-turbulence interaction subgrid models can *only* be realized in 3D. Consequently, all longer-time simulations, in which the bubble enters a turbulent state have been run in 3D with Cartesian geometry with a turbulence-flame interaction model to capture enhanced burning on subgrid scales. All 3D simulations were performed both with and without the turbulence-flame interaction (TFI) model (described below), thereby spanning a range of possible outcomes on the flame propagation resulting from unresolved turbulence. Test 2D simulations in cylindrical coordinates led to unphysical behavior in the turbulent phase, including spurious surface protuberances burning in the radial direction and thus significantly altering the simulation outcomes in comparison to 3D models. Artificial outcomes were particularly significant for runs with ignition points close to the center of mass of the white dwarf, where unphysical burning in the radial direction has the largest impact.

Our Cartesian domain extends from $-6.5536 \times 10^5 \text{ km}$ to $+6.5536 \times 10^5 \text{ km}$ in each direction, with a maximal refinement down to $\Delta = 4 \text{ km}$. We employ several refinement criteria, which are designed to follow the nuclear burning of the models at high resolution, while also minimizing the resolution in the very low density regions outside the white dwarf itself. Our simulations seek to

maintain the highest resolution in the burning region behind the flame surface, and employ a standard density gradient criterion to refine when the density gradient parameter exceeds 0.1, and derefines when it is beneath 0.0375. Further refinement criteria seek to derefine in the fluff and in regions outside of active burning, derefining one level if the energy generation rate is lower than $5 \times 10^{17} \text{ erg g}^{-1} \text{ cm}^{-3}$, and completely to level one if the density is below 10^3 g cm^{-3} . Except for their resolution and threshold, these criteria are the same as in Townsley et al. (2009). Furthermore, because the ejected ash continues to expand over time, the computational cost of following the ejected ash grows without bound. Consequently, we impose an additional derefinement outside a radius of 4000 km to $\Delta = 128 \text{ km}$, which only impacts the ejected mass. We increased this derefinement radius to 6000 km for offsets $r_0 \lesssim 20 \text{ km}$, where the pre-expansion can reach similar radii.

The single flame bubble’s initial size is limited by the hydrodynamic resolution of our simulations. At a resolution of $\Delta = 4 \text{ km}$ for the flame front, we assume an initial spherical shape with radius is set to $R_0 = 16 \text{ km}$. In order for this to be a reasonable assumption, a self-consistent evolution since appearance of the hot spot should yield a negligible velocity profile and a self-similar evolution preserving sphericity as discussed in Vladimirova (2007).

The consistency of assuming a spherical ignition point can be assessed with simple physical arguments. The flame polishing scale $\lambda_{\text{fp}} = 4\pi S_l^2 / (Ag)$, below which perturbations on the surface are polished out (Timmes & Woosley 1992), implies that even if the initial ignition was non-spherical it would become spherical soon afterwards. An explicit numerical test confirming this was performed by Malone et al. (2014). Later perturbations to the sphericity can arise from a turbulent background flow and the buoyant rise. The background flow is small compared to the laminar flame speed of $\sim 100 \text{ km/s}$, so that sphericity should initially be sustained. The impact of the buoyant rise on sphericity is closely linked to the question of a negligible initial velocity field, whose amplitude however increases as the bubble starts to rise. We assume the velocity field to become relevant when the velocity from the gravitational acceleration g reaches the order of the laminar velocity, the stretching scale l_{fl} . This should approximately corresponds to $l_{\text{fl}} = 2S_l^2 / (Ag)$ (Malone et al. 2014), which primarily depends on the offset near the white dwarf’s center. A is the Atwood number of fuel and ash density. Note that this criterion is stricter by a factor of 2π compared to the criterion for sphericity due to perturbations: The flame bubble is expected to stretch radially

before the wrinkles in the flame front are not polished out anymore. Alternatively to above estimator for l_{fl} , we integrate the flame’s evolution based on (Fisher & Jumper 2015) to determine when the bubble’s velocity reaches the laminar flame speed, which is shown in Table 1. Only at small radial bubble offsets r_0 from the center, which we are particularly interested in, fulfill this condition. This length scales with r_0^{-1} and therefore the condition allows large bubbles at low offsets. As Fisher & Jumper (2015) argue that there is a critical offset at which the deflagration will burn through the core, vastly changing the overall deflagration yield and thus its possible detonation, a completely self-consistent evolution would be desirable at these offsets. However, we are effectively limited by the required computational resources and resolution. As an alternative for such self-consistent treatment, we evolve 2D models for the linear phase, where deviations to 3D outcomes should be negligible, which we can resolve sufficiently well.

We incorporate a turbulence-flame interaction model presented in Jackson et al. (2014) implementing a specific model of power-law wrinkling based on that proposed by Charlette et al. (2002). The reaction front is modeled by a reaction-diffusion front which propagates with a speed based upon the estimated physical features of the wrinkled physical flame whose width is, for most of the interior of the WD, many orders of magnitude smaller than the computational grid scale. Due to the interaction of turbulence with the flame, the location of the reaction front, as coarsened to a filter scale Δ consisting of a few grid cells, is approximated to propagate at a turbulent flame speed $s_t = \Xi s_l$, where s_l is the physical laminar flame speed, and Ξ is called the wrinkling factor. The wrinkling is given by

$$\Xi = \left(1 + \frac{\Delta}{\eta_c}\right)^{1/3}, \quad (1)$$

where η_c is the cutoff scale for wrinkling, and is dependent upon local properties of both the turbulence and the physical flame. In this model, η_c is the inverse of the mean curvature of the flame surface, and is determined by assuming equilibrium between subgrid flame surface creation due to wrinkling by the turbulence and flame surface destruction by flame surface propagation and diffusion. This turbulence-flame interaction model leads to a turbulent flame speed s_t that is approximately equal to the characteristic speed of turbulent fluctuations on the filter scale, u'_{Δ} at intermediate densities, 10^8 - 10^9 g cm^{-3} , as can be seen in Figure 4 in Jackson et al. (2014). The turbulent flame speed falls off to the laminar flame speed at lower densities where the flame is too thick and slow to support wrinkling. At

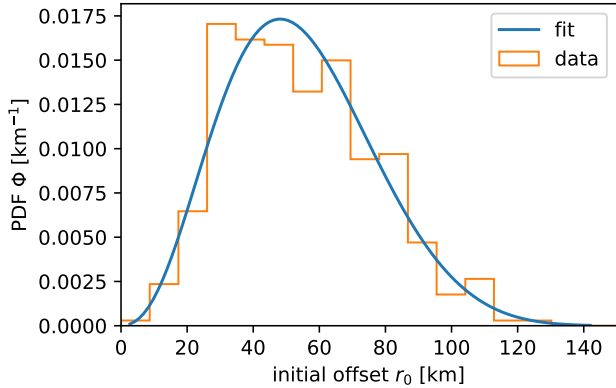


Figure 1. Radial hot spot distribution and fit function for raw data used in (Nonaka et al. 2012).

high densities where the flame is effectively polished by the high laminar speeds, the turbulent flame speed also approaches to the laminar flame speed value. Performing the calculation of the cutoff scale for wrinkling, η_c , requires a measurement of the turbulence on the filter scale, u'_Δ , and makes the physical assumption that the subgrid turbulence is homogeneous, isotropic, and follows Kolmogorov’s theory on the filter scale. As shown by Zingale et al. (2005), buoyancy-driven turbulence becomes increasingly homogeneous and isotropic on small scales, implying the last assumption is valid provided the filter scale is sufficiently small.

From Nonaka et al. (2012) we obtain the probability density $P(r)$ of hot spots forming at a certain distance from the center of mass. Using the raw data and the same methodology, we create a histogram for such distribution and a fit to this distribution, see Figure 1. Shown is the probability density function per unit length. Under the assumption that the probability density per volume only mildly changes near the center of mass, this implies a $P(r)dr \propto r^2 dr$ scaling at low offsets due to the shrinking volume available for hot spots to occur. While not exactly fulfilling this consideration, we obtain a reasonable fit using a β -distribution, obtaining an expectation value of $\langle r_0 \rangle = 48$ km and a probability of 2.2% for hot spots forming at $r_0 < 16$ km, the critical ignition radius determined by Fisher & Jumper (2015).

We simulate the outcomes of varying ignition offsets for the given progenitor according to the this probability distribution and choose a representative range of initial offsets with an initial bubble radius of $R_0 = 16$ km shown in Table 2. We utilize both 2D and 3D simulations. The size of the initial bubble is naturally limited by the simulation resolution. As demonstrated analytically in (Fisher & Jumper 2015), the flame bubble’s

Table 1. Performed 2D runs with a maximal resolution of $\Delta = 0.25$ km and initial radius of 2 km.

Offset (km)	λ_{fp} (km)	l_{fl} (km)
4	353.6	40.9
10	141.4	27.2
20	70.7	17.6
50	28.3	8.2

dynamics vastly change at low initial offsets. We employ 2D simulations to investigate the initial stages of the bubble dynamics at very high resolution. Moving to 2D is a reasonable strategy in this case, as we are only interested in the initial, linear phase. In 2D, we employ a maximal resolution of 0.25 km and an initial bubble radius of 2 km, at initial offsets ranging from 0 – 50 km as listed in Table 1.

The 3D simulations are evolved until they can undergo a detonation as GCD. The precise conditions under which a DDT may arise are still a matter of active investigation, though recent three-dimensional simulations may shed further light on this issue (Poludnenko et al. 2011; Fisher et al. 2018). We adopt conservative criteria for detonation initiation based upon studies of the the Zel’dovich gradient mechanism (Seitenzahl et al. 2009), which demonstrate that the critical length above temperatures $\simeq 2 \times 10^9$ K at a density 10^7 g cm $^{-3}$ become of order 1 km, and a detonation is deemed likely. Further, in this paper, we evolve all 3D models within the context of the GCD scenario. As discussed in the introduction, current *ab initio* calculations point towards offset single-point ignitions, which favor both the GCD and DDT scenario over pure deflagrations. Because the GCD model involves further evolution post-bubble breakout, it generally predicts a greater deflagration energy release than the DDT model, for an otherwise identical WD progenitor and flame bubble ignition model. Consequently, consideration of the GCD model yields a lower limit for the mass of ^{56}Ni due to a lower central density ρ_c at the time of detonation, in comparison to DDT models.

Artificial detonations can occur due to temperature oscillations arising as numerical artifacts from degenerate stellar equation of state coupled with hydrodynamics close to discontinuities (Zingale & Katz 2015). These oscillations are particularly striking during the flame bubble’s buoyant rise. In order to prevent detonations arising from these artifacts, we restrict detonations to occur in the southern hemisphere ($z < 0$ km).

Table 2. Performed 3D runs with a maximal resolution of $\Delta = 4$ km.

Offset (km)	TFI	t_{det} (s)	M_{Ni56} (M_{\odot})
0	✓/✗	failed ^a /failed ^a	0.56/0.35
16	✓/✗	3.70/2.92	1.08/1.05
20	✓/✗	3.34/3.27	1.12/1.06
32	✓/✗	2.61/2.54	1.14/1.14
40	✓/✗	3.06/2.42	1.09/1.13
50	✓/✗	2.48/2.31	1.14/1.20
100	✓/✗	2.26/2.12	1.21/1.20
125	✓/✗	2.21/2.08	1.22/1.20

^aModel fails to detonate.

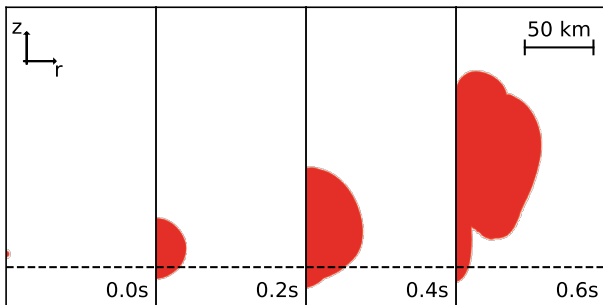


Figure 2. Deflagration phase during the first 0.6 s for a 2D model with 10 km offset, 2 km initial radius and a resolution of 0.25 km. The dashed line shows $z = 0$ km. On the coordinate axis r denotes $\sqrt{x^2 + y^2}$.

3. RESULTS

We first discuss the early phase of bubble evolution. The early linear phase of evolution is similar in both 2D and 3D, so we investigate the early linear evolution in high-resolution 2D models and compare these against semi-analytic predictions. We then move on to examine the subsequent nonlinear evolution through breakout and detonation in full 3D, which we also evolve starting with the linear phase, but at lower resolution.

3.1. Early Linear Evolution in 2D

Figure 2 shows the slices of the flame bubble’s evolution in its laminar phase for $r_0 = 10$ km. The burned material grows spherically as long as the buoyant velocity is small and the bubble’s size stays below the flame polishing scale. As the bubble grows, the acceleration for material at the northern and southern flame front start to differ and the bubble becomes elongated along the initial offset’s direction until a plume forms at the northern front. Interestingly, the southern flame front’s

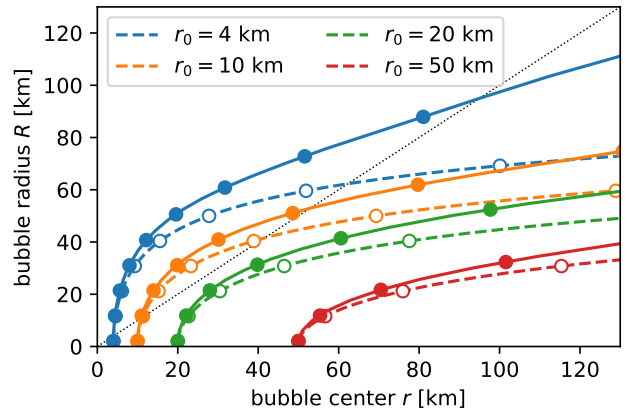


Figure 3. Bubble evolutionary tracks shown for both 2D hydrodynamic simulations as well as for the analytic solution in (Fisher & Jumper 2015). The plot shows the bubble radius R versus offset radius r . The evolution of different initial offsets r_0 is shown as the solid curve for simulations and as the dashed curve for the analytical solution. The dots represent time steps of 0.1 s, starting with 0.0 s. States above the dotted line have burned through the white dwarf’s center of mass.

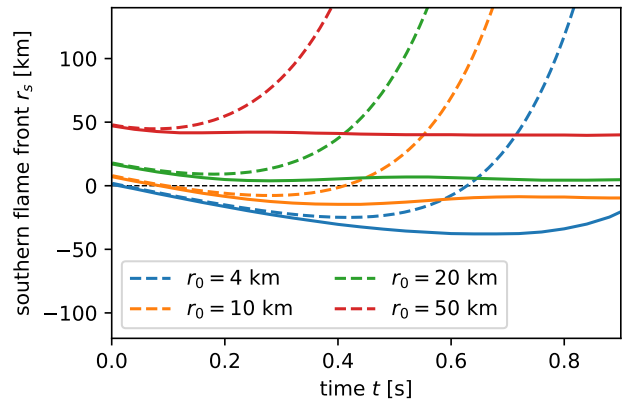


Figure 4. Position of the southern flame front r_s as a function of time t after ignition. Line style and color are chosen as in Figure 3.

laminar speed seems to be countered by the background flow from the buoyant rise at the northern front.

In Figure 3, we show the evolution of the flame bubble’s radius $R(r)$ as a function of the bubble offset $r(t)$. For the simulation data, the volume-equivalent spherical radius ($R = \sqrt[3]{3V/4\pi}$) deduced from the burned volume V is shown. We compare our results from the initial phase of linear growth with the analytic model presented in (Fisher & Jumper 2015) and find them to be in good agreement for the first tenths of seconds, particularly for

larger initial offsets. The analytic description starts to fail as the velocity from the buoyant rise becomes inhomogeneous across the bubble, effectively stretching the bubble due to a lower speed at the southern flame front. Figure 4 shows the position of the southern flame front’s position for the analytic and numerical evolution, which start to differ as the analytic solution does not incorporate an inhomogeneous velocity/acceleration field. The resulting elongation gives rise to a stem being left behind the rising plume at the northern front. Even when the southern flame front crosses the center of mass it will not buoyantly rise towards the opposite pole but is confined close to the center of mass on the relevant timescale due to the background flow caused by the buoyant rise of the ash on the northern hemisphere.

3.2. Non-linear Evolution and Detonation

With formation of a rising plume the evolution becomes non-linear and depends on the imposed flame model as presented in Section 2. To capture the flame’s turbulent rise, we evolve 3D models from ignition to detonation for the parameters listed in Table 2. As we find the 3D runs to remain mostly symmetric, we show slices in the z - x plane restricted by $x \geq 0$ km and $y = 0$ km. Figure 5 and 6 show the evolution of the white dwarf for 20 km and 100 km offset. Figure 7 also shows the evolution of a 20 km offset model, but without enhanced burning that the prior two models use. Because the evolutionary timescales for each run depend on the initial conditions chosen, the slices for each run are chosen with respect to the state of the flame, and not in absolute time. In particular, in each plot, the first frame shows the breakout of the flame at the star’s surface. The next frame depicts the post-breakout flame crossing the $z = 0$ equator on the star’s surface. The last frame shows the model just prior to detonation across from the point of breakout.

While low offsets also have a slightly larger distance to the WD’s surface, the evolution of shown models demonstrate the delay to breakout in comparison to larger offsets due to the smaller buoyant force near the center of mass, increasing the breakout time by roughly 0.3 s for $r_0 = 20$ km over $r_0 = 100$ km. Smaller initial offsets, lead to a slightly increased plume size both in radial and tangential direction with respect to the center of mass across different initial offsets.

After breakout, the flame front travels around the white dwarf and eventually reaches the point opposing the point of breakout. Material of the envelope is pushed in front of this flame front into this opposing point. At larger offsets than 40 km, such as the shown 100 km run, the ram pressure building up suffices to trigger a

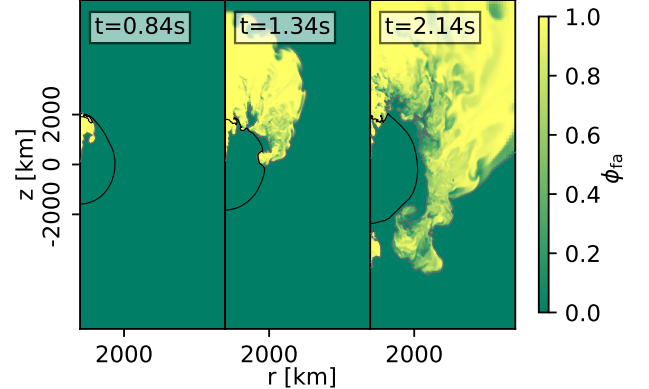


Figure 5. Time series for run with enhanced burning at an offset of 100 km in three stages: Breakout, equator crossing and prior to detonation. Slices are shown in the positive quadrant of the x - z plane with $y = 0$ km with $r = \sqrt{x^2 + y^2}$. The colormap indicates the amount of burned material ϕ_{fa} . The solid line shows the density contour for $\rho = 10^7$ g cm $^{-3}$.

detonation before the ash reaches the opposing point. For smaller offsets than roughly 40 km, such as the runs with an initial offset of 20 km, the ram pressure is insufficient to trigger a detonation upon the flame reaching the opposite pole and a detonation only occurs after a subsequent partial recontraction of the white dwarf delaying the detonation. For some offsets lower than the shown 20 km, the white dwarf might not detonate upon recontraction either.

The difference of the enhanced burning model seems to be only moderate for the shown slices at offset $r_0 = 20$ km. The evolutionary phases represented by the slices coincide between flame models, while without enhanced burning a larger fraction of the material ejected from the white dwarf seems to be burned.

Figure 8 shows the estimated ^{56}Ni yield over time relative to the time of ignition. The ^{56}Ni yield in each model is obtained from the electron mass fraction Y_e , and by assuming the neutronization of IGE occurs in equal parts by mass of ^{54}Fe and ^{58}Ni for all Y_e , which holds within 2% in tabulated yields from previous models (Meakin et al. 2009; Townsley et al. 2009). The rapid increase of $M_{\text{Ni}56}$ occurring at $t \gtrsim 2.0$ s indicates the onset of detonation, except for offset $r_0 = 0$ km, where a large growth sets in at $t = 1.0$ s due to turbulent deflagration.

We classify the progenitor’s evolution into three different classes: failed, GCD and PGCD. The PGCD scenario introduced by (Jordan et al. 2012) shows a strong recontraction phase ($2 \cdot t_{det,GCD} \lesssim t_{det,PGCD}$) due to a significantly increased deflagration yield from a many-

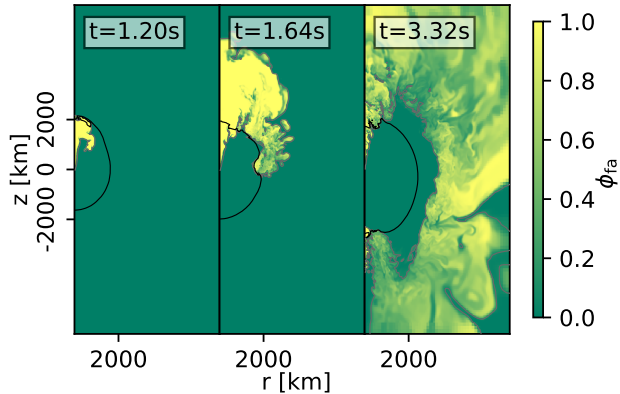


Figure 6. Time series for run with enhanced burning at an offset of 20 km analogous to Figure 5.

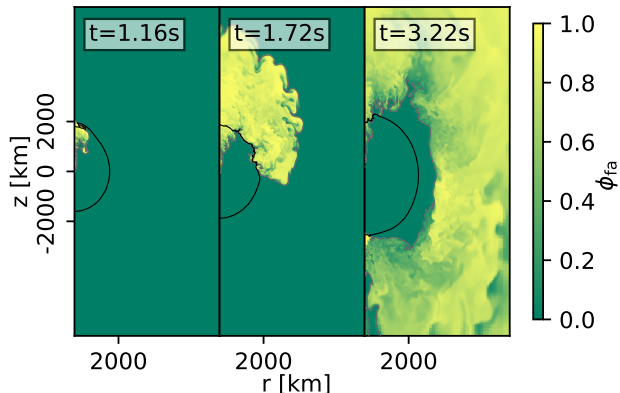


Figure 7. Time series for run without enhanced burning at an offset of 20 km analogous to Figure 5.

bubble-ignition setup. Given the smaller deflagration yields in our simulations due to the single ignition hot spot, PGCDs here only show a mild recontraction (as e.g. indicated by the evolution of the central density), making the transition between PGCDs and GCDs gradual: Sometimes, there is no detonation upon buildup of ram pressure but only when the fuel-ash mixture reaches the southern pole even if no clear recontraction is present. We therefore do not impose a binary criterion between those scenarios.

As Figure 9 and Table 2 show, the ^{56}Ni yield seems to converge towards roughly $1.21 M_{\odot}$ at large offsets $r \gtrsim 100$ km with the progenitors undergoing the GCD scenario. As suspected by (Fisher & Jumper 2015) the ^{56}Ni yield decreases with lower initial offset as visualized in Figure 9. For runs $\lesssim 40$ km a transition towards PGCD-like scenarios takes place. The transition is not monotonic, but has a stochastic component whether the

ram pressure from the initial deflagration will suffice for an imminent detonation or not. For example, in our simulations a 32 km offset suffices for a GCD, despite the onset of a PGCD already at $r_0 = 40$ km.

At some point we might expect the PGCD scenario to fail. However, we lack the spatial resolution at very small radial offsets to determine the location of this transition. Thus, we are left with the artificial case of central ignition for which the ^{56}Ni yield from deflagration increases to $0.56 M_{\odot}/0.35 M_{\odot}$ (TFI/no TFI), depending on the flame model. However, there is no detonation so that the total yield drops to these values as compared to higher initial offsets. Due to the numerical expense of resolving the energy generating regions at maximal resolution with AMR, we had to derefine to a maximal resolution of $\Delta = 8$ km at $t = 2.00/1.82$ s for the no TFI/TFI scenarios with $r_0 = 0$ km. Based on our parameter sampling, the transition from PGCD to failed must occur at $0 \text{ km} < r_0 < 16$ km for the chosen progenitor.

At large offsets, the yields with and without enhanced burning model vary only marginally. However, at lower offsets the enhanced burning significantly adds to the ^{56}Ni yield, particularly for the failed events where differences add up to 60%, but also for PGCD events in the order of up to 10%.

3.3. Likelihood of ^{56}Ni Yields

We next compute the probability distribution of $M_{\text{Ni}56}$ outcomes for the presented GCD SD channel models. The transformation from the hot spot probability distribution $P(r_0)$ to the probability distribution $P(M_{\text{Ni}56})$ of ^{56}Ni outcomes is given as

$$P(M_{\text{Ni}56}) = \sum_{r_0 \in g^{-1}(M_{\text{Ni}56})} \frac{P(r_0)}{|g'(r_0)|}. \quad (2)$$

Here $g(r_0) \equiv M_{\text{Ni}56}(r_0)$ is the amount of ^{56}Ni produced as a function of offset radius r_0 . $P(r_0)$ is the hot spot distribution found in (Zingale et al. 2011) shown in Figure 1. This relationship may be derived from Bayes' Theorem with minimal assumptions. We start with

$$P(M_{\text{Ni}56}|r_0)P(r_0) = P(r_0|M_{\text{Ni}56})P(M_{\text{Ni}56}), \quad (3)$$

and assume a simplification that the ^{56}Ni yield is solely determined by the offset position, leaving out possible uncertainties from velocity flow and early bifurcations arising in the turbulent phase, one finds

$$\begin{aligned} P(M_{\text{Ni}56}|r_0) &= \delta(g_{M_{\text{Ni}56}}(r_0) - M_{\text{Ni}56}), \\ P(r_0|M_{\text{Ni}56}) &= \delta(r_0 - g^{-1}(M_{\text{Ni}56})), \end{aligned}$$

Here $\delta(x)$ is the Dirac delta distribution. Finally, using the identity

$$\delta(f(x)) = \sum_i \frac{\delta(x - x_i)}{|f'(x_i)|}, \quad (4)$$

where we sum over the roots x_i of $f(x)$, we can rewrite equation 3 as equation (2).

Even for a very similar stellar structure, we expect bifurcations arising from the turbulent nature of the flame bubble’s buoyant rise affecting the final ^{56}Ni yield. In our computations, we see a similar phenomenon from slight offset changes and perturbations of the initial flame bubble. Therefore, the yields we obtained do not need to follow a monotonous relationship as only one possible realization is drawn at a given offset. Given the numerical expense, neither can we evaluate multiple runs at the same offset with slightly modified stellar structure or flame bubble, nor can we afford to run more models at different offsets. However, if deemed significant, additional parameters such as varied background velocity field, could easily be incorporated by marginalizing over such parameters. With our limited data sample we nevertheless try to obtain insights into the resulting spread of ^{56}Ni yields given the stochastic nature of the initial ignition offset. To do so, we impose a strictly monotonous fit function for $M_{\text{Ni}56}(r_0)$ with an asymptotic yield at high offsets r_0 for which we use

$$y(r_0) = \frac{y_{\text{max}} + \Delta y}{2} + \frac{y_{\text{max}} - \Delta y}{2} \cdot \tanh(s \cdot (r_0 - r_s)), \quad (5)$$

where y_{max} is the asymptotic yield at high offsets, Δy the spread between the two asymptotic branches, r_s the position of the turning point and s characterizes the sensitivity of the ^{56}Ni yield with respect to the initial offset r_0 . We fix the asymptotic yield to the approximate value y_{max} found earlier.

The resulting distributions $P(M_{\text{Ni}56})$ for our progenitor model with and without enhanced burning are shown in Figure 10. We show the probability distributions for events with offsets larger than 16 km, accounting for 97.8% of the ignitions. The distribution shows a slightly larger spread for the non-TFI models due to the lower ^{56}Ni yield at low ignition offsets. Nevertheless, we find that the majority of ignitions result in a very confined ^{56}Ni yield.

For given hot spot distribution $P(r_0)$ and the outcomes $M_{\text{Ni}56}(r_0)$ of the simulated progenitor, we get a stochastic spread $P(M_{\text{Ni}56})$ outcomes that is strongly favors overluminous events with a ^{56}Ni yield of $\sim 1.2 M_{\odot}$ with a standard deviation of $\sigma \sim 0.03$. However, the

total spread in outcomes of detonating models $\delta = \max(M_{\text{Ni}56}(r_0)) - \min(M_{\text{Ni}56}(r_0))$ due to the stochasticity of hot spots forming is significantly larger. We are limited by the hydrodynamic resolution, but find that $\delta \gtrsim 0.2 M_{\odot}$.

We find $\sigma \ll \delta$ for both TFI and no TFI models as the ^{56}Ni yield is already close to asymptotic value of $1.21 M_{\odot}$ at radii $r_0 \sim 50$ km, which is the most likely point of ignition for the assumed hot spot distribution. For a hot spot distribution peaking closer to the WD’s center of mass, the standard deviation could be significantly higher. The exact shape of the left tail of the distribution is highly uncertain as it depends on the chosen fit function given our sparse sampling. Similarly, we expect modeling uncertainties, e.g. due to the lack of a velocity field, to propagate most severely into the ^{56}Ni yield and the resulting probability distribution at low offset radii as the buoyant evolution can be strongly enhanced or delayed. Other stochastic parameters, such as the state of the WD’s velocity field, were not considered, but would have to be marginalized over to obtain probability distribution in a more elaborate study.

4. DISCUSSION

We have shown how the ignition offset probability distribution directly links to a range of SNe Ia outcomes, parameterized by the ^{56}Ni yield. This range of SNe Ia outcomes is intrinsically connected to the turbulent convective velocity field in the near- M_{Ch} WD progenitor, which causes the ignition of the SD channel to be inherently stochastic and unpredictable. The physics of the SD channel is complex and is subject to numerous modeling uncertainties: the pre-WD stellar evolution, accretion from the companion, possibly impacting the WD initial composition and structure, the physics of the simmering phase leading up to ignition, and the physics of turbulent nuclear burning and detonation. In the following, we discuss this range of modeling uncertainties and to what extent each of these effects may impact our conclusions.

Another crucial piece of physics underlying both the simmering phase and the nuclear burning within the SNe Ia is the rate for C12 + C12 fusion. Recent experiments have measured this reaction rate for the first time for center-of-mass energies in the range of 0.8 - 2.5 MeV, and demonstrated using the Trojan horse method, an enhancement in the cross sections by as much as a factor of 25 in a key temperature range relevant to SNe Ia (Tumino et al. 2018). While this work has been contested by other authors (Mukhamedzhanov & Pang 2018) (and subsequently rebutted – Tumino et al. (2018)), and will ultimately await additional confirmation, it is important

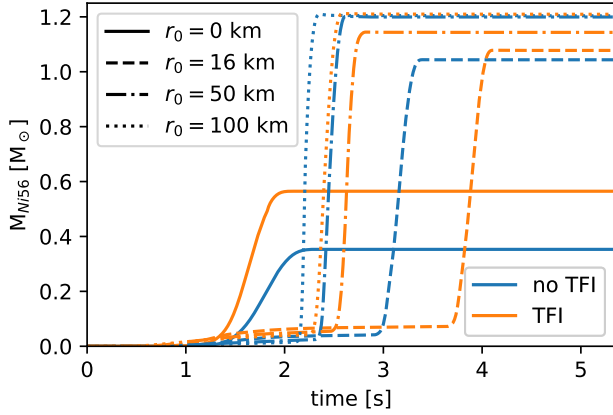


Figure 8. Nickel 56 yield $M_{\text{Ni}56}$ over time t after ignition for the 3D simulations at selected initial offsets r_0 with and without TFI.

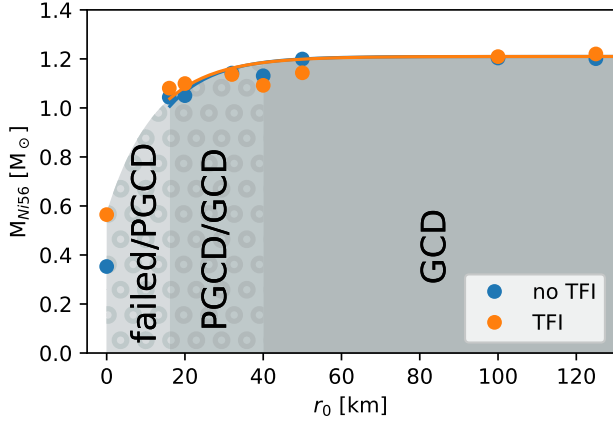


Figure 9. Nickel 56 yields at different offsets in 3D with and without enhanced burning including the arctan-fit. Shaded regions mark offsets resulting in GCD/PGCD/failed scenarios according to their label. Additionally hatched regions mark transitions between scenarios due to computational limitations and classification ambiguities (see text).

to recognize the possible impact which uncertainties in this key reaction rate may have upon the SNe Ia modeling. A higher reaction rate would increase the flame speed and might particularly change the $M_{\text{Ni}56}$ outcomes at low offsets where the buoyant evolution is most sensitive to changes of our fiducial model.

In this work, we have incorporated the statistical distribution of ignition points drawn from actual three-dimensional simulations of the convective simmering phase of near- M_{Ch} WDs leading up to ignition. While this approach has clear advantages over the majority of prior work, which typically adopted ignition points

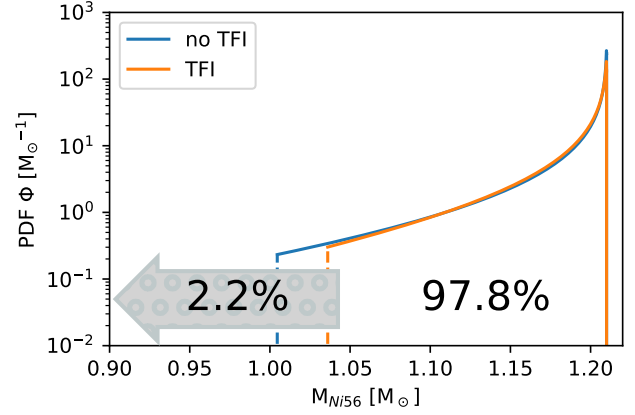


Figure 10. Probability density function for Nickel 56 yields based on simulations and the hot spot probability density function.

in an arbitrary fashion, it is nonetheless still limited by the fact that there has only been one high-quality three-dimensional simmering phase simulation in a single WD progenitor completed to date. The simulation has been performed at increasing resolution, and the distribution of hot spot offsets appears to be converged (Zingale et al. 2011; Nonaka et al. 2012; Malone et al. 2014). However, it is conceivable that the distribution of hot spots could be more centrally-condensed in WD progenitors with higher central density.

The mechanism underlying the initiation of detonation plays an important role in SNe Ia theory, and much effort has focused upon whether the detonation mechanism in a near- M_{Ch} SD scenario is a DDT or GCD (Röpke et al. 2007b; Seitenzahl et al. 2016; Dave et al. 2017). For example, because the DDT detonates prior to bubble breakout, the stratification of the ^{56}Ni and IGEs is generally more centrally condensed, in broader agreement with observations of high $M_{\text{Ni}56}$, overluminous SNe Ia like 91T (Seitenzahl et al. 2016). In the current work, we have focused upon the GCD mechanism in our simulations in inferring the intrinsic variation of the ^{56}Ni production resulting from stochastic ignition. However, if we were to have instead adopted a DDT criterion for detonation initiation, the ^{56}Ni distribution would be even more heavily left-skewed. This is because, given identically the same WD progenitor and ignition point, the DDT detonates prior to breakout, and consequently always results in a less pre-expanded WD progenitor than a GCD (Dave et al. 2017). As a result, the conclusion that the stochastic variance in ^{56}Ni yields is small, and the mean ^{56}Ni yield is large, is not qualitatively modified under the DDT scenario.

In this work, we have begun with a quiescent WD, although the ignition arises in the WD interior, which is itself convective, and as a consequence of the transport of angular momentum from the accretion stream, may itself be rotating. Indeed, recent work has shown that the effect of rotation may be significant enough to weaken the convergence in the detonation region of a classical GCD (García-Senz et al. 2016), although a PGCD might still be possible. Furthermore, at low ignition offsets, the magnitude of the initial convective velocity field may have an impact on the early flame bubble’s evolution, and thus the ^{56}Ni yield. As we start our simulations with zero velocity, this adds an additional uncertainty in the resulting $M_{\text{Ni}56}$ distribution. On the one hand, there is turbulence on small scales, distorting the flame front early on. Expected velocities for this are small (~ 10 km/s) with regard to the laminar flame speed (~ 100 km/s), so that the flame bubble’s sphericity is still mostly unaffected until broken by its buoyant rise. Minor shifts in a possible failed-to-detonated transition radius might be to be expected. On the other hand, there is a possibility of the ignition point to occur in a larger convective flow. If such hot spots form in convectively outward moving regions as found by (Nonaka et al. 2012), this will further decrease the probability for ignitions that burn through the WD’s center. (Malone et al. 2014) ran a series of numerical simulations similar to our setup for the deflagration phase, but additionally include a comparison of a setup with self-consistent convective velocity field and one without any velocity field. In these simulations, the authors find the influence of the initial flow field to increase as the initial ignition point is set closer to the center of mass, particularly for an exactly centered ignition.

Stellar composition influences the final nucleosynthetic yield of a SD SNe Ia through a variety of effects. The CNO metals of the WD stellar progenitor ultimately yield ^{22}Ne during He burning. Umeda et al. (1999) suggested that a variation in the carbon abundance within the progenitor WD in the single-degenerate channel would impact the production of ^{56}Ni . In particular, Umeda et al. (1999) conjectured that WDs with a richer C/O ratio would lead to a more turbulent flame, an earlier transition from deflagration to detonation at higher densities, and hence a greater production of ^{56}Ni . Timmes et al. (2003) demonstrated both analytically and numerically that the neutron excess carried by ^{22}Ne results in a decrease in the $M_{\text{Ni}56}$ of the SN Ia event, in direct proportion to the abundance of ^{22}Ne . Townsley et al. (2009) further considered a range of additional compositional effects influencing the final nucleosynthetic yields, including the ignition density, the en-

ergy release, the flame speed, the WD structure, and the density at which a possible deflagration-to-detonation transition arises. The simulations with ^{22}Ne mass fractions increasing from 0 to 0.02, which were run long enough to determine a final ^{56}Ni yield, demonstrate that the combination of these effects result in a roughly 10% decrease in $M_{\text{Ni}56}$. Similarly, we expect a slight decrease in $M_{\text{Ni}56}$ based on complementary work by Jackson et al. (2010) investigating the impact of the ^{22}Ne content on the DDT density and the resulting ^{56}Ni mass.

Computational simulations of single-degenerate SNe Ia have subsequently explored the influence of varying the C/O ratio within the progenitor WD in the context of the DDT model (Krueger et al. 2010; Ohlmann et al. 2014). These investigations have demonstrated that higher C/O ratios yield more energetic and more luminous SNe Ia.

Taken together, this body of work on SD SNe Ia generally supports the view that stellar progenitor C/O ratio and metallicity play a role in determining the brightness of a SN Ia event. However, at the same time, these models have demonstrated that additional free parameters, including both the number and distribution of ignition points, as well as the DDT transition density, have a combined effect on the explosion energy comparable to that of the C/O ratio and stellar progenitor metallicity. Moreover, based upon this body of work, the combined influence of both a decrease in the C/O ratio and an increase in the stellar progenitor metallicity from the values assumed here (50/50 and 0, respectively), would result in a 10% - 20% decrease in the ^{56}Ni yields, which would quantitatively impact our predicted $M_{\text{Ni}56}$ distribution, but not alone yield a distribution more closely resembling normal SNe Ia.

Most simulation models of near- M_{Ch} WDs adopt a central density $\rho_c \simeq 2 \times 10^9$ g cm $^{-3}$, as we have in this paper. Because the electron capture rates are highly sensitive to the density, higher-central density WDs generally produce greater amounts of stable IGE, and a lower ^{56}Ni yield. Higher central density WDs significantly overproduce (relative to solar) a range of neutron-rich isotopes, including ^{50}Ti , ^{54}Cr , ^{58}Fe , and ^{62}Ni , and as a consequence, were generally excluded from consideration as near- M_{Ch} WD progenitors (Meyer et al. 1996; Nomoto et al. 1997; Woosley 1997; Brachwitz et al. 2000). However, if SD near- M_{Ch} WDs constitute a small fraction of all SNe Ia, such high-central density WDs may not be rare occurrences. If the central density of the near- M_{Ch} WD is indeed higher than $\rho_c \simeq 2 \times 10^9$ g cm $^{-3}$, then the flame speed and the consequent deflagration energy release can be greater than considered here. This can in turn lead to greater pre-expansion and

a reduced amount of ^{56}Ni as shown in 2D simulations (Krueger et al. 2012; Dave et al. 2017), possibly consistent with a normal or even a failed SNe Ia. However, the qualitative outcome of an increased higher central density can vary as shown by Seitenzahl et al. (2011). In their 3D numerical study of the DDT scenario, the authors of the latter study show that the central density is only a secondary parameter. However, their study assumed multipoint ignition over a wide range of ignition kernels. When single point ignitions are adopted, increased electron capture rates at higher central densities lead to higher abundances of neutron-rich iron peak elements at the expense of ^{56}Ni (Dave et al. 2017).

5. CONCLUSIONS

In this paper, we investigated the impact of a single initial ignition’s offset r_0 for a single ignition point of a deflagration flame bubble in a fiducial 50/50 C/O WD with a central density of $2.2 \times 10^9 \text{ g cm}^{-3}$ and an adiabatic temperature profile leading up to Type Ia supernovae in the GCD scenario.

We showed that a transition to failed SNe Ia (i.e. those events lacking a GCD) occurs as r_0 falls below some offset below 16 km. Even for those white dwarfs detonating, the ^{56}Ni yield spawns a range of outcomes changing by 10 – 20% with a decreasing yield as r_0 approach the radius where no detonation is triggered.

Summarizing our key conclusions:

1. Stochastic range of outcomes. For chosen progenitor this corresponds to a spread of $\delta \gtrsim 0.2 M_\odot$ for detonating models, even though the $M_{\text{Ni}56}$ distribution is strongly left-skewed so that low $M_{\text{Ni}56}$ are unlikely for the given probability distribution. This range of outcomes is stochastic and will add onto other variations from the different progenitors’ stellar structure and evolution.
2. For non-centered ignitions, all ignitions lead up to an overluminous SNe Ia. We do not find a viable scenario from a single bubble ignition leading to a normal Type Ia for the progenitor used here, which is also commonly referenced in literature. This disfavors single degenerate progenitors as a contributing channel to failed and normal type Ia SNe. If this channel was to contribute to failed and normal type Ia supernovae, this would require readjustment and better understanding of the stellar structure and evolution, and flame dynamics.
3. (Quasi-)symmetric deflagrations around the center of mass, as commonly used in numerical studies, are most likely artificial constructs: Ignitions very close to the center are rare as shown by Nonaka et al. (2012) and even if such events occur, a strong asymmetry evolves as a background flow in direction of the outermost flame front counteracts the burning into other directions as numerically demonstrated here for offsets as small as 4 km. However, future in-depth studies on the likelihood of multi-ignition occurrences and their correlations with the turbulent velocity field might leave room for rare occurrences of symmetric deflagrations.

Acknowledgements The authors thank Mike Zingale for generously providing the simulation data from his group’s convective simmering phase models, which was used in Figure 1. The authors thank Pranav Dave and Rahul Kashyap for insightful conversations. RTF also thanks the Institute for Theory and Computation at the Harvard-Smithsonian Center for Astrophysics for visiting support during which a portion of this work was undertaken. CB acknowledges support from the Deutscher Akademischer Austauschdienst (DAAD). RTF acknowledges support from NASA ATP award 80NSSC18K1013. This work used the Extreme Science and Engineering Discovery Environment (XSEDE) Stampede 2 supercomputer at the University of Texas at Austin’s Texas Advanced Computing Center through allocation TG-AST100038. XSEDE is supported by National Science Foundation grant number ACI-1548562 (Towns et al. 2014).

We use a modified version of the FLASH code 4.3 (Fryxell et al. 2000), which was in part developed by the DOE NNSA-ASC OASCR Flash Center at the University of Chicago, for our simulations including the SN Ia modeling presented in Townsley et al. (2016). The authors have made use of Frank Timmes’ hot white dwarf progenitor (http://cococubed.asu.edu/code_pages/adiabatic_white_dwarf.shtml). For our analysis, we acknowledge use of the Python programming language (Van Rossum & de Boer 1991), the use of the Numpy (van der Walt et al. 2011), IPython (Perez & Granger 2007), and Matplotlib (Hunter 2007) packages. Our analysis and plots strongly benefited from the use of the yt package (Turk et al. 2011).

REFERENCES

- Arnett, W. D. 1969, *Ap&SS*, 5, 180
- Brachwitz, F., Dean, D. J., Hix, W. R., et al. 2000, *ApJ*, 536, 934

- Branch, D., Livio, M., Yungelson, L. R., Boffi, F. R., & Baron, E. 1995, 107, 1019
- Cao, Y., Kulkarni, S. R., Howell, D. A., et al. 2015, *Nature*, 521, 328
- Charlette, F., Meneveau, C., & Veynante, D. 2002, *Combustion and Flame*, 131, 159
- Childress, M. J., Hillier, D. J., Seitzzahl, I., et al. 2015, *MNRAS*, 454, 3816
- Couch, S. M., Graziani, C., & Flocke, N. 2013, *ApJ*, 778, 181
- Dave, P., Kashyap, R., Fisher, R., et al. 2017, *ApJ*, 841, 58
- Fisher, R., & Jumper, K. 2015, *ApJ*, 805, 150
- Fisher, R. T., Mozumdar, P., & Casabona, G. O. 2018, *ArXiv e-prints*, arXiv:1807.03786
- Fryxell, B., Olson, K., Ricker, P., et al. 2000, *The Astrophysical Journal Supplement Series*, 131, 273–334
- García-Senz, D., & Bravo, E. 2005, *A&A*, 430, 585
- García-Senz, D., Cabezón, R. M., Domínguez, I., & Thielemann, F. K. 2016, *ApJ*, 819, 132
- García-Senz, D., & Woosley, S. E. 1995, *ApJ*, 454, 895
- Hillebrandt, W., Sim, S. A., & Röpke, F. K. 2007, *Astronomy and Astrophysics*, 465, L17
- Hunter, J. D. 2007, *Computing in Science Engineering*, 9, 90
- Isern, J., García-Berro, E., Külebi, B., & Lorén-Aguilar, P. 2017, *ApJL*, 836, L28
- Jackson, A. P., Calder, A. C., Townsley, D. M., et al. 2010, *ApJ*, 720, 99
- Jackson, A. P., Townsley, D. M., & Calder, A. C. 2014, *The Astrophysical Journal*, 784, 174
- Jiang, J.-a., Doi, M., Maeda, K., & Shigeyama, T. 2018, *ArXiv e-prints*, arXiv:1808.06343
- Jordan, IV, G. C., Fisher, R. T., Townsley, D. M., et al. 2008, *ApJ*, 681, 1448
- Jordan, IV, G. C., Graziani, C., Fisher, R. T., et al. 2012, *ApJ*, 759, 53
- Kasen, D. 2010, *ApJ*, 708, 1025
- Katsuda, S., Mori, K., Maeda, K., et al. 2015, *ApJ*, 808, 49
- Khokhlov, A. M. 1991, *A&A*, 245, 114
- Kraichnan, R. H. 1967, *The Physics of Fluids*, 10, 1417
- Kromer, M., Fink, M., Stanishev, V., et al. 2013, *MNRAS*, 429, 2287
- Kromer, M., Fremling, C., Pakmor, R., et al. 2016, *MNRAS*, 459, 4428
- Krueger, B. K., Jackson, A. P., Calder, A. C., et al. 2012, *ApJ*, 757, 175
- Krueger, B. K., Jackson, A. P., Townsley, D. M., et al. 2010, *ApJL*, 719, L5
- Malone, C. M., Nonaka, A., Woosley, S. E., et al. 2014, *ApJ*, 782, 11
- Maoz, D., & Mannucci, F. 2012, *Publications of the Astronomical Society of Australia*, 29, 447
- Maoz, D., Mannucci, F., & Nelemans, G. 2014, *ARA&A*, 52, 107
- Marion, G. H., Brown, P. J., Vinkó, J., et al. 2016, *ApJ*, 820, 92
- Martínez-Rodríguez, H., Badenes, C., Yamaguchi, H., et al. 2017, *The Astrophysical Journal*, 843, 35
- Meakin, C. A., Seitzzahl, I., Townsley, D., et al. 2009, *ApJ*, 693, 1188
- Meyer, B. S., Krishnan, T. D., & Clayton, D. D. 1996, *ApJ*, 462, 825
- Mori, K., Famiano, M. A., Kajino, T., et al. 2018, *ArXiv e-prints*, arXiv:1808.03222
- Mukhamedzhanov, A. M., & Pang, D. Y. 2018, *ArXiv e-prints*, arXiv:1806.08828
- Nomoto, K., Iwamoto, K., Nakasato, N., et al. 1997, *Nuclear Physics A*, 621, 467
- Nomoto, K., Thielemann, F.-K., & Yokoi, K. 1984, *ApJ*, 286, 644
- Nonaka, A., Aspden, A. J., Zingale, M., et al. 2012, *ApJ*, 745, 73
- Ohlmann, S. T., Kromer, M., Fink, M., et al. 2014, *A&A*, 572, A57
- Perez, F., & Granger, B. E. 2007, *Computing in Science Engineering*, 9, 21
- Phillips, M. M. 1993, *ApJL*, 413, L105
- Plewa, T., Calder, A. C., & Lamb, D. Q. 2004, *ApJL*, 612, L37
- Poludnenko, A. Y., Gardiner, T. A., & Oran, E. S. 2011, *Physical Review Letters*, 107, 054501
- Röpke, F. K., Hillebrandt, W., Schmidt, W., et al. 2007a, *ApJ*, 668, 1132
- Röpke, F. K., Woosley, S. E., & Hillebrandt, W. 2007b, *ApJ*, 660, 1344
- Seitzzahl, I. R., Ciaraldi-Schoolmann, F., & Röpke, F. K. 2011, *Monthly Notices of the Royal Astronomical Society*, 414, 2709
- Seitzzahl, I. R., Meakin, C. A., Townsley, D. M., Lamb, D. Q., & Truran, J. W. 2009, *ApJ*, 696, 515
- Seitzzahl, I. R., Ciaraldi-Schoolmann, F., Röpke, F. K., et al. 2013, *Monthly Notices of the Royal Astronomical Society*, 429, 1156
- Seitzzahl, I. R., Kromer, M., Ohlmann, S. T., et al. 2016, *A&A*, 592, A57
- Shappee, B. J., Piro, A. L., Stanek, K. Z., et al. 2018, *ApJ*, 855, 6
- Timmes, F. X., Brown, E. F., & Truran, J. W. 2003, *ApJL*, 590, L83

- Timmes, F. X., & Swesty, F. D. 2000, *The Astrophysical Journal Supplement Series*, 126, 501–516
- Timmes, F. X., & Woosley, S. E. 1992, *ApJ*, 396, 649
- Towns, J., Cockerill, T., Dahan, M., et al. 2014, *Computing in Science Engineering*, 16, 62
- Townsley, D. M., Calder, A. C., Asida, S. M., et al. 2007, *ApJ*, 668, 1118
- Townsley, D. M., Jackson, A. P., Calder, A. C., et al. 2009, *ApJ*, 701, 1582
- Townsley, D. M., Miles, B. J., Timmes, F. X., Calder, A. C., & Brown, E. F. 2016, *ApJS*, 225, 3
- Tumino, A., Spitaleri, C., La Cognata, M., et al. 2018, *Nature*, 557, 687
- Tumino, A., Spitaleri, C., La Cognata, M., et al. 2018, *ArXiv e-prints*, arXiv:1807.06148
- Turk, M. J., Smith, B. D., Oishi, J. S., et al. 2011, *The Astrophysical Journal Supplement Series*, 192, 9
- Umeda, H., Nomoto, K., Kobayashi, C., Hachisu, I., & Kato, M. 1999, *ApJL*, 522, L43
- van der Walt, S., Colbert, S. C., & Varoquaux, G. 2011, *Computing in Science Engineering*, 13, 22
- Van Rossum, G., & de Boer, J. 1991, *CWI Quarterly*, 4, 283
- Vladimirova, N. 2007, 11, 377
- Whelan, J., & Iben, Jr., I. 1973, *ApJ*, 186, 1007
- Woosley, S. E. 1997, *ApJ*, 476, 801
- Woosley, S. E., Wunsch, S., & Kuhlen, M. 2004, *ApJ*, 607, 921
- Yamaguchi, H., Badenes, C., Petre, R., et al. 2014, *ApJL*, 785, L27
- Yamaguchi, H., Badenes, C., Foster, A. R., et al. 2015, *ApJL*, 801, L31
- Zingale, M., & Katz, M. P. 2015, 216, 31
- Zingale, M., Nonaka, A., Almgren, A. S., et al. 2011, *ApJ*, 740, 8
- Zingale, M., Woosley, S. E., Rendleman, C. A., Day, M. S., & Bell, J. B. 2005, *ApJ*, 632, 1021